HAL
open science

Multiphysics Simulation Combining Large-Eddy Simulation, Wall Heat Conduction and Radiative Energy Transfer to Predict Wall Temperature Induced by a Confined Premixed Swirling Flame

Chai Koren, Ronan Vicquelin, Olivier Gicquel

To cite this version:

Chai Koren, Ronan Vicquelin, Olivier Gicquel. Multiphysics Simulation Combining Large-Eddy Simulation, Wall Heat Conduction and Radiative Energy Transfer to Predict Wall Temperature Induced by a Confined Premixed Swirling Flame. Flow, Turbulence and Combustion, 2018, 101 (1), pp.77-102. 10.1007/s10494-018-9895-5 . hal-01744260

HAL Id: hal-01744260

https://hal.science/hal-01744260

Submitted on 27 Mar 2018

HAL is a multi-disciplinary open access archive for the deposit and dissemination of scientific research documents, whether they are published or not. The documents may come from teaching and research institutions in France or abroad, or from public or private research centers.

L'archive ouverte pluridisciplinaire **HAL**, est destinée au dépôt et à la diffusion de documents scientifiques de niveau recherche, publiés ou non, émanant des établissements d'enseignement et de recherche français ou étrangers, des laboratoires publics ou privés.

Multiphysics simulation combining large-eddy simulation, wall heat conduction and radiative energy transfer to predict wall temperature induced by a confined premixed swirling flame

Chai Koren · Ronan Vicquelin · Olivier Gicquel

Abstract A multi-physics simulation combining large-eddy simulation, conjugate heat transfer and radiative heat transfer is used to predict the wall temperature field of a confined premixed swirling flame operating under atmospheric pressure. The combustion model accounts for the effect of enthalpy defect on the flame structure whose stabilization is here sensitive to the wall heat losses. The conjugate heat transfer is accounted for by solving the heat conduction within the combustor walls and with the Hybrid-Cell Neumann-Dirichlet coupling method, enabling to dynamically adapt the coupling period. The latter coupling procedure is enhanced to determine statistics (mean, RMS, ...) in a permanent regime accurately and efficiently thanks to an acceleration technique which is derived and validated. The exact radiative heat transfer equation is solved with an advanced Monte Carlo method with a local control of the statistical error. The coupled simulation is carried out with or without accounting for radiation. Excellent results for the wall temperature are achieved by the fully coupled simulation which are then further analyzed in terms of radiative effects, global energy budget and fluctuations of wall heat flux and temperature.

Keywords Large Eddy Simulation · Turbulent Combustion · Conjugate Heat Transfer · Thermal Radiation · Monte-Carlo

Chai Koren · Ronan Vicquelin · Olivier Gicquel
Laboratoire EM2C, CNRS
CentraleSupélec
Université Paris-Saclay
Grande Voie des Vignes, 92295
Chatenay-Malabry cedex, France
E-mail: ronan.vicquelin@centralesupelec.fr

Chai Koren
Air Liquide
Centre de Recherche Paris-Saclay
1 Chemin de la Porte des Loges, 78350
Les-Loges-en-Josas, France

1 Introduction

The increasing number of applications of large-eddy simulations (LES) in practical combustor configurations [34,16] outlines the growing maturity of such methods to simulate turbulent reactive flows. While subgrid-scale modeling efforts are still ongoing, the range of applications of such high-fidelity computations widens to new horizons such as multiphysics simulations of conjugate heat transfer (CHT). Several applications to turbine blades have been reported [9,10] as well as combustion cases [22,2,31]. The accurate prediction of heat flux and temperature at the combustor wall requires accounting for the coupling between the turbulent reactive flow, the heat conduction within the walls and the radiative energy transfer. The later phenomenon, radiation, has also been coupled to reactive LES in different studies [23,41,39,2]. Combining LES with conjugate heat transfer and thermal radiation in a multiphysics framework can nowadays be envisioned and enables a state-of-the-art estimation of wall heat loads. Besides, coupling LES with radiative heat transfer enables to alleviate most of the issues of Turbulence-Radiation Interaction (TRI) [6,7] which is significant in RANS simulations. Nevertheless, subgrid-scale TRI effects remain neglected in the present study but modelling studies have recently emerged [43,19]. Such a pioneering high-fidelity approach has been presented in [2] and applied a helicopter combustor while describing the radiation properties with a global model. The coupling frequency with the radiation solver was however strongly limited. Nevertheless, accurate unsteady simulations such as LES to predict unsteady wall heat loads is very promising to determine thermal fatigue in combustors as recently developed in the nuclear engineering community [29,28,14].

The employed multiphysics methodology relies on separate solvers to treat each physical phenomenon. To be affordable, conjugate heat transfer with LES must be carried out on massively parallel clusters. In these unsteady simulations, both flow and heat conduction solvers exchange data at their interface regularly after a prescribed coupling time step Δt_{cpl}. The optimal value of the latter quantity is not known. The recently developed Hybrid-Cell Neumann-Dirichlet (HCND) method [27] is considered to determine this coupling time step dynamically from an accuracy tolerance. This makes the HCND method relevant to high-fidelity unsteady numerical studies of conjugate heat transfer when considering a direct numerical or large-eddy simulation in the flow field. However, an issue to deal with in unsteady simulations of CHT problems is the slow conduction process such that the transient heating or cooling of a solid part to its permanent state requires to simulate a physical time which is not affordable. The term *permanent regime* is used to denote the final behavior of the system after an initial transient phase. In a general case, this final state (in turbulent or oscillatory flows) remains unsteady and is characterized by a spectrum of harmonics. Steady conditions denote conditions that do not present any temporal variations. The issue of the slow conductive transient is usually alleviated by artificially accelerating the physical transient to reach sooner the permanent regime which is still unsteady in a pulsated or turbulent flow. Several techniques have been proposed in the literature to carry out such an acceleration [11,9,22,2,21,20]. The HCND being based on synchronized data, it is not compatible (see details in Sec. 2) with the established techniques for acceleration. A first study is therefore dedicated to derive an acceleration method for the HCND coupling approach in order to keep its benefits (accuracy control and

self-adaptive determination of coupling time step) while determining permanent regime statistics in turbulent flows.

A multiphysics simulation is then applied to a confined premixed swirling flame [18,17] whose stabilization has been shown to be sensitive to the wall conditions as in other similar flames [38,45,40,8]. On the combustion modeling side, this requires to describe the effect of non-adiabaticity due to heat losses on the flame structure and its stabilization [24,47,32,33]. The flame has previously been simulated successfully in a non-coupled and stand-alone LES based on a non-adiabatic F-TACLES (Filtered Tabulated Chemistry for LES) model [33]. The wall temperature profiles were then specified from the experimental ones that were measured by Laser Induced Phosphorescence. The main objective of this study is to predict this wall temperature field in order to retrieve the combustor characteristics in terms of flame stabilization and wall heat losses without any prior knowledge from the experimental data. To do so, the proposed multiphysics simulation aims at describing each physical phenomenon as accurately as possible: i) large-eddy simulation with a combustion model that accounts for the effect of enthalpy defect on the flame structure, ii) an efficient Monte-Carlo solver with detailed radiative properties and controlled accuracy, and iii) a self-adaptive coupling procedure for conjugate heat transfer to compute accurately steady and unsteady components of the solid domain temperature. This provides a high-fidelity coupled simulation which, to the best of the authors' knowledge, is unprecedented in the investigated realistic configuration.

The article is organized in three main sections. Section 2 deals first with the derivation and validation of the accelerated variant of Hybrid-Cell Neumann-Dirichlet method. The setup of the numerical solvers and physical models to simulate the investigated confined premixed swirling flame are given in Sec. 3. Finally, coupled results with or without accounting for radiative energy transfer are detailed an analyzed in Sec. 4.

2 Hybrid-Cell Neumann-Dirichlet method and acceleration of the transient regime

Among the different techniques to accelerate the thermal transient, a first example is the coupling of an unsteady flow solver with a steady solid heat transfer solver [11]. By doing so, the mean fields are obtained at a low computational cost but this approach is limited to steady-state computations and cannot grant access to the temperature and heat flux fluctuations in the wall. A second approach is the desynchronization method [9,22,2] which can be used with fully unsteady coupled simulations. In this method, codes are no longer synchronized in terms of physical time: while the flow solver simulates a physical time of Δt_{cpl} the solid heat transfer solver simulates a physical time of $\alpha \Delta t_{cpl}$ where $\alpha \approx 100 - 500$. This methodology provides an efficient and robust way to compute the mean temperature and wall heat flux fields on the interface boundary. However, the employed coupling approach that is HCND is not consistent with the desynchronization formalism. Moreover, by modifying the frequencies perceived by the solid, such a technique amplifies the level of heat load fluctuations. Once the permanent regime is reached, one could stop the acceleration algorithm but the transient from the erroneous to the unperturbed permanent fluctuations is characterized by a large conduction

time scale, which brings back to the original issue. The objective in this section is therefore to derive an artificial acceleration method for the HCND approach that does not perturb the predicted statistics (mean and rms) in permanent regime while keeping the advantages of the original coupling method. The Hybrid-Cell Neumann-Dirichlet method is first briefly presented before being enhanced to artificially accelerate the transient heating or cooling of the structure. Validations are carried out on a 1D unsteady CHT problem.

2.1 Hybrid-Cell Neumann-Dirichlet method

The Hybrid-Cell Neumann-Dirichlet (HCND) method [27] has been derived for target applications which are coupled DNS/LES of unsteady CHT. For the sake of accuracy of such coupled high-fidelity methods, the coupling time step between communications of separate solvers is self-adapted. This is done by considering hybrid cells around the solid-fluid interface (see Fig. 1) in order to derive the following ordinary differential equation for the boundary temperature:

$$\frac{dT_{bnd}}{dt} = -\frac{\Phi_{f,bnd} + \Phi_{s,bnd}}{V_f \rho_f c_{pf} + V_s \rho_s c_{ps}}. \tag{1}$$

The coupling approach is based on a layer of such hybrid cells at the boundary. The integrated heat flux over all internal faces in the solid domain of the hybrid cell is denoted $\Phi_{s,bnd}$, and $\Phi_{f,bnd}$ in the fluid. Both quantities are provided by the flow and solid solvers. Temperature Dirichlet boundary conditions are then provided for the flow and solid heat transfer solvers. Thanks to this formulation, an automatic determination of the coupling time step is achieved by controlling the numerical integration error. As detailed in [27], given an estimated numerical error from two temporal integration schemes, a controller adapts the coupling time step for the next coupling stage. Undesired variations in the coupling time step due to the coupled dynamics of the controller and the considered equation system solved with variable time steps must be prevented. This is why a robust PID controller [42] is considered and has been shown to work satisfactorily [27]. This achieved control of the numerical error also ensures the numerical stability of the coupling procedure. The only parameter is then a prescribed tolerance to control the numerical accuracy of the coupling method.

2.2 Superposition of mean and fluctuating parts to afford computing permanent regime statistics

As highlighted in the introduction, the discrepancy between the fluid and solid time scales leads to a huge need in computational resources: computing the transient heating or cooling of a combustion chamber requires simulating a very large physical time. The desynchronization technique is widely used in CHT studies with LES [9, 22, 2]. However, HCND coupling method is not compatible with such a procedure since the boundary temperature is determined by an ordinary differential equation which requires temporal synchronization of heat fluxes from both solvers. For this reason, an acceleration method based on a similar approach to [21, 20] is derived: the temperature field inside the walls is described as the superposition of

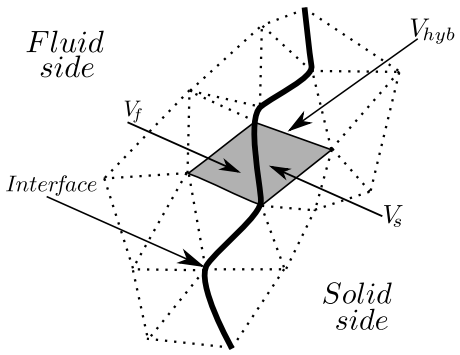

Fig. 1 One hybrid cell of volume V_{hyb} (in grey) is the union of fluid and solid cells of volume V_f and V_s located on each side of the interface.

a steady and a transient component: $T_s = \widehat{T}_s + T'_s$. Each component is then solved using the adequate heat transfer equation:

$$0 = \nabla.(\lambda_s \nabla \widehat{T}_s) \tag{2}$$

$$\rho_s c_{p,s} \frac{\partial T'_s}{\partial t} = \nabla.(\lambda_s \nabla T'_s) \tag{3}$$

The instantaneous wall heat flux on the fluid side, $\Phi_{f,bnd}$, is also split into two components: A mean wall heat flux $\widehat{\Phi}_{f,bnd}$ and a fluctuating heat flux $\Phi'_{f,bnd}$ such that

$$\Phi'_{f,bnd} = \Phi_{f,bnd} - \widehat{\Phi}_{f,bnd}. \tag{4}$$

Solving Eq. 2 is accomplished by using the mean wall heat flux $\widehat{\Phi}_{f,bnd}$ as a boundary condition on the shared interface, and yields the solid mean temperature field of $\widehat{T}_s$ including the interface mean temperature $\widehat{T}_{bnd}$. In the unsteady fluid solver, the estimated mean wall heat flux at a time τ is computed by time averaging the instantaneous wall heat flux:

$$\widehat{\Phi}_{f,bnd}(\tau) = \frac{1}{\tau} \int_0^\tau \Phi_{f,bnd}(t) dt \tag{5}$$

As the cumulating duration τ in this integral increases, the computed quantity $\widehat{\Phi}_{f,bnd}(\tau)$ converges to the steady mean flux $\overline{\Phi}_{f,bnd}$. The unsteady fluctuating solid temperature equation, Eq. 3, is coupled to a fluctuating variant of the boundary temperature equation, Eq. 1,

$$\frac{dT'_{bnd}}{dt} = -\frac{\Phi'_{f,bnd} + \Phi'_{s,bnd}}{V_f \rho_f c_{pf} + V_s \rho_s c_{ps}}. \tag{6}$$

following the usual HCND coupling method, which still self-adapts the coupling time step given a prescribed tolerance. Finally, the instantaneous boundary temperature, used as a boundary condition by the flow solver, is obtained by summing both parts:

$$T_{bnd} = \widehat{T}_{bnd} + T'_{bnd} \tag{7}$$

Table 1 Properties of both mediums considered in 1D test cases: Thermal conductivity, density, thermal capacity at constant pressure

Inconel steel		Burnt gases	
λ_s	11.70 W/m/K	λ_f	0.4496 W/m/K
ρ_s	8510.0 kg/m^3	ρ_f	1.154 kg/m^3
$c_{p,s}$	439.0 J/kg/K	$c_{p,f}$	1738 J/kg/K

In [21,20], the considered mean/fluctuation splitting is carried out on all considered Fourier modes. The fundamental mode, *i.e.* the steady state, is solved with a steady heat transfer equation solver while the unsteady heat conduction is solved for other spectral modes in the frequency-domain. With the introduced splitting, keeping a time-domain resolution to describe all types of fluctuations enables to account for a single unsteady equation which is solved numerically with a controlled accuracy. As in [21,20], the acceleration to a permanent regime by disregarding the slow solid conduction process results from providing the mean heat flux $\widehat{\Phi}_{f,bnd}$, which converges within several flow time scales, directly as a boundary condition to the steady conduction problem in Eq. 2. Let us explain this carefully: The superposition principle of a mean state and a fluctuating part is exact as long that the boundary condition applied to Eq. 2 is the exact steady mean flux. During the simulated initial transient, it is not the case since the cumulative average in Eq. 5 (that ultimately reaches a mean steady state) is not converged. Hence, Eq. 2 is forced in a quasi-steady behavior where the applied non-converged wall heat flux is then instantaneously equilibrated in the solid thermal state. This is how the physical transient is artificially accelerated. Ultimately, the cumulative average in Eq. 5 converges to a steady mean value. This is when the strict validity of the superposition becomes valid and the fluctuations in the reached permanent regime are then not impacted by the acceleration method. Once $\widehat{\Phi}_{f,bnd}$ is converged, Eq. 2 also yields the exact mean steady solution in the solid.

2.3 1D validation of the accelerated coupling

The HCND coupling methodology combined with the acceleration method of the thermal transient is first tested on a one-dimensional test case used in [27].The test case consists of two coupled one-dimensional codes, each solving the unsteady heat equation in each medium. The fluid and solid mediums of size L_f and L_s, respectively, are: The burnt gases of oxycombustion at a 20-bars pressure on the one hand, and an Inconel steel on the other hand. Properties of both mediums are given in table 1. The configuration is shown in Fig. 2: The interface is located at the axial position $x = 0$ with the fluid medium on the negative x-values and the solid medium at the positive x-values. Boundary conditions are applied at both extreme edges of the domain: at $x = -L_f$, the fluid temperature fluctuates following a temporal sine wave of frequency f_{ext},

$$T_{f,ext} = T(x = -L_f, t) = T_0(1 + 0.1\sin(2\pi f_{ext} t)) + T_{s,ext} \tag{8}$$

with $T_0 = 1000$ K, while at $x = L_s$, the solid's outer boundary $T_{s,ext}$ is a fixed temperature equal to the initial mean temperature in both mediums: 293 K.

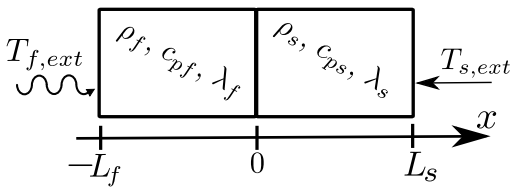

Fig. 2 One-dimensional test case configuration. The length L_f of the fluid part is 1 mm while the length L_s of the solid part is 1 mm. Reproduced from [27], copyright ©2017 Elsevier Masson SAS, all rights reserved.

The evolution of the resulting interface temperature along time is plotted in Fig. 3. The order of magnitude of the transient time to permanent regime can in fact be estimated by the characteristic conduction time scale $\tau_{cond} = \delta^2/a_s$ in the solid, where δ is a solid characteristic length and $a_s = \lambda_s/(\rho_s c_{p_s})$ the solid thermal diffusivity. The estimated physical transient time is $\tau_{cond} = 0.32$ s where δ is taken as the solid domain size L_s and $a_s = 3.1 \times 10^{-6}$ m^2/s. This gives a dimensionless time $\tau_{cond} \cdot f_{ext} \approx 30$ which is consistent with the non-accelerated solution shown in Fig. 3. The fluctuations amplitude in Fig. 3 is two orders of magnitude smaller than the one entering at $x = -L_f$. This effect can be attributed to the value of the thermal activity ratio K ($= 4.78\,10^{-3}$ in this case), defined as:

$$K = \sqrt{\frac{\rho_f c_{pf} \lambda_f}{\rho_s c_{ps} \lambda_s}}. \tag{9}$$

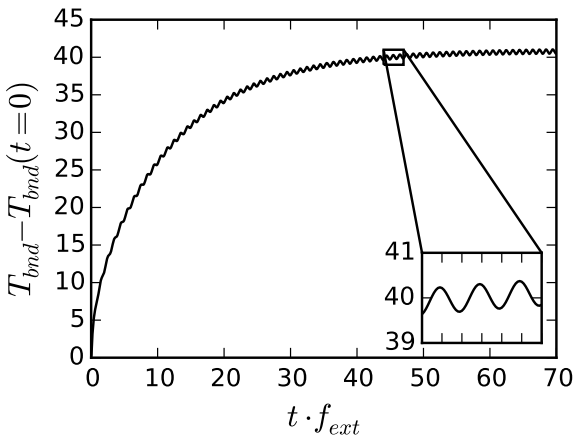

Fig. 3 Temporal evolution of the boundary temperature for $f_{ext} = 100$ Hz. Reproduced from [27], copyright ©2017 Elsevier Masson SAS, all rights reserved.

Results for the described superposition approach are compared with a reference solution (sufficiently refined to neglect discretization errors) without any artificial

acceleration (here, affordable in 1D) and with a standard Neumann-Dirichlet coupling method accelerated by the desynchronization method [9,22,2] with the factor $\alpha = 10$ and $\alpha = 100$. For a better assessment of the methods, the boundary temperature evolution is split into two components. The first one is the evolution of the pseudo-mean temperature $\widehat{T}_{bnd}$ defined as in Eq. 5 at the fluid/solid interface. Tracking its evolution allows a better vision of the convergence speed of the calculated mean temperature field towards its steady value. The second component studied is the fluctuating part of the boundary temperature, generated by the oscillating outer boundary condition.

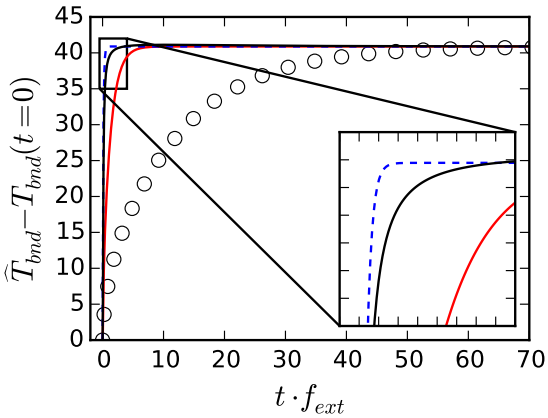

Fig. 4 Temporal evolution of the mean component of the boundary temperature. Circles: Non-accelerated reference case. Red solid line: Neumann-Dirichlet coupling approach with a desynchronization factor $\alpha = 10$. Blue dashed line: Neumann-Dirichlet coupling approach with a desynchronization factor $\alpha = 100$. Black solid line: The HCND coupling approach with the derived acceleration method based on the superposition of mean and fluctuating states. Case conditions: $f_{ext} = 100$ Hz and prescribed tolerance $\eta = 5\%$ for the HCND approach.

The mean component of the boundary temperature is plotted in Fig. 4. The reference solution shows that the transient heating determined by the solid time scale corresponds approximatively to fifty periods of the chosen value of f_{ext}. Desynchronizing the solid physical time from the one seen in the fluid enables to reach the steady plateau much faster. With different values of the desynchronization factor α, convergence can be made arbitrarily short although one must still pay attention to the numerical stability of the coupling method [9]. The proposed method also enables to quickly reach the steady value of the boundary temperature, much sooner than in the reference solution. The plateau reached by the symbols on the right of Fig. 4 is the steady mean temperature to retrieve. Both acceleration methods predict accurately this mean value after the accelerated transient.

Figure 5 shows the unsteady part of the interface temperature. According to the reference solution, the imposed fluctuations yield an amplitude of approximatively 1 Kelvin at the interface. A known weakness of the desynchronization method is observed: The heat flux fluctuations received by the solid wall have a frequency

which is scaled by α and hence a response amplitude which is multiplied by $\sqrt{\alpha}$ [22]. On the other hand, the proposed superposition approach of the mean and unsteady parts provides an excellent agreement after an initial transient time. These first five or six signal periods have indeed been influenced by the pseudo-mean temperature value which has not converged yet. Once the permanent regime is reached, the predicted fluctuations are accurate, which is the purpose of the acceleration method.

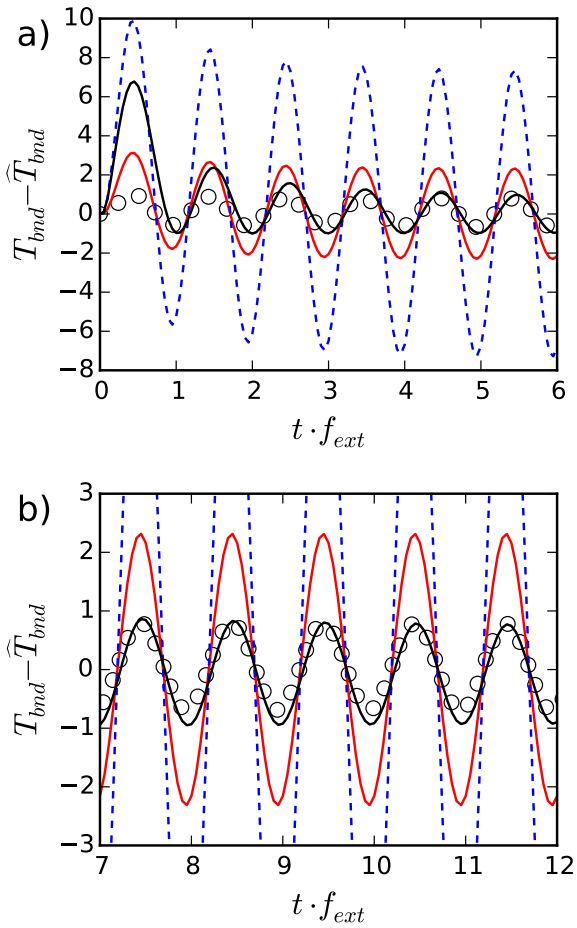

Fig. 5 Temporal evolution of the unsteady component of the boundary temperature. (a) $t \cdot f_{ext}$ between 0 and 6. (b) Zoom in the permanent regime for $t \cdot f_{ext}$ between 7 and 12. Same line and symbol conventions as in Fig. 4.

The combination of the proposed acceleration method and HCND coupling method successfully predicts the steady wall temperature and heat flux in the permanent regime without perturbing their unsteady contributions and while automatically determining the coupling time step. The validation in 1D cases of

this approach has been illustrated for one value of the frequency f_{ext}. The method actually works equally well for other frequencies. It is now applied to the study of a confined turbulent flame in the next section.

3 Experimental and numerical setups of the confined premixed swirling flame

3.1 Experimental setup

The experimental setup used to validate the proposed coupling strategy was studied experimentally by Guiberti *et al.* [17,33]. A schematic view of the setup is available in Fig. 6. The combustion chamber height H is 250 mm with a square cross-section 92 mm x 92 mm. It encloses of a swirled premixed flame, where the fuel is a mixture of H_2 and CH_4 (60% and 40% in volume, respectively). The equivalence ratio is 0.7, the swirl number is set to 0.4 and the fresh gases temperature is 293 K. The corresponding thermal power of the flame is 4 kW.

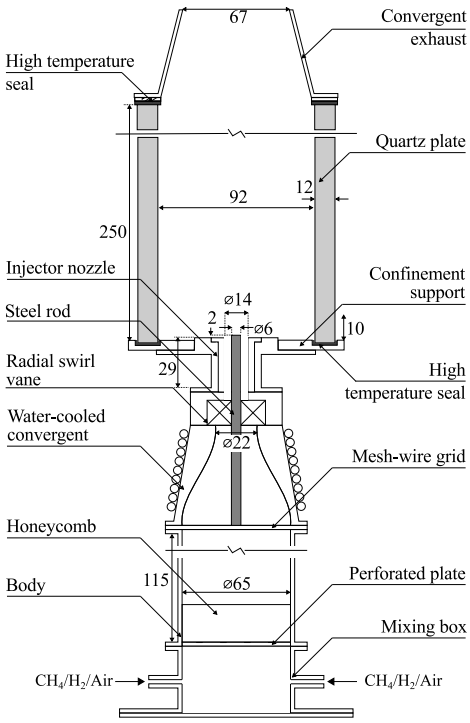

Fig. 6 Schematic view of the studied burner [18,17,33].

The numerical setup and modeling of the reactive flow, described in the next section, has previously been validated [33] against measurements of velocity profiles, OH* chemiluminescence and OH-PLIF. Wall temperature measurements de-

termined by Laser Induced Phosphorescence which were then prescribed as boundary conditions in the simulation are the target data to be predicted by a multiphysics approach. Such data are available for one of the four combustor's quartz windows in a 51 mm x 58 mm zone.

3.2 Numerical solvers

The multi-physics simulation is carried out by coupling separate solvers that describe the turbulent reactive flow, radiative heat transfer and wall heat transfer. The three solvers are detailed below.

3.2.1 Turbulent reactive flow

The employed setup for large-eddy simulation of reactive flows is identical to [33]: the solver, the mesh and the models' parameters are the same. In particular, the swirler is not included in the computational domain of the considered reactive simulations and the inlet profiles have been prescribed from another LES of the full non-reactive case. The YALES2 LES solver [35,30] is based on a low Mach-number assumption and uses finite-volume formalism with fourth order time integration and space discretization schemes. The pressure Poisson equation is solved using a deflated conjugate gradient method [30]. The subgrid Reynolds stresses are modelled with the SIGMA model [37], an extension of the wall adapting local eddy viscosity (WALE) model [36]. In particular, both SIGMA and WALE models keep the proper near-wall cubic behavior of the streamwise velocity in wall-resolved simulations of turbulent boundary layers. Outside of the flame region, the unresolved scalar turbulent fluxes are determined with constant turbulent Schmidt and Prandtl numbers.

The chemistry and turbulent combustion are described with the tabulated chemistry model F-TACLES [13,1] and Charlette *et al.* [5] subgrid-scale flame wrinkling model. For the considered configuration which features heat losses, the effect of enthalpy variations on the combustion model is accounted for with a non-adiabatic extension [32,12] of the F-TACLES model. For perfectly-premixed conditions as in the present case, the different physical variables are only tabulated as a function of a progress variable Y_c and a heat losses correction coefficient [32].

A first stand-alone LES was conducted using wall laws to account for unresolved boundary layers. It showed a maximal value of cell size in wall units $y^+ \approx 1.5$ (similar in terms of x^+ and z^+). The grid is then fine enough for the investigated case and, combined with the SIGMA subgrid-model, it allows a wall-resolved LES approach.

3.2.2 Gases radiation

The burnt gases thermal radiation is accounted for by solving the radiative transfer equation without taking into account subgrid turbulence-radiation interaction. The spectral radiative emission and absorption are therefore computed from the LES filtered fields of temperature and composition in the radiative transfer equation. This is done with a Monte-Carlo method implemented in the RAINIER solver, an in-house parallel code of the EM2C laboratory. Such methods are deemed

the most accurate after deterministic ray tracing. They can account for complex geometries and spectral properties. Here, a cK method based on accurate parameters directly obtained from a high-resolution database [44] enables a detailed description of radiative properties of CO_2 and H_2O. In order to afford coupling such Monte-Carlo methods with LES, several features must be met: parallel scalability, local accuracy control and fast convergence. The RAINIER code uses an Optimized Emission-based Reciprocity Monte-Carlo method (OERM) [49]. Scalability is strongly enhanced by treating each mesh point independently from the others with a local monitoring of the statistical error. Such a property is inherited by the ERM (Emission-based Reciprocity Monte-Carlo) approach [46]. ERM is however penalized by a slow statistical convergence in cold absorbing regions. This limitation is overcome by OERM using a frequency distribution function based on the emission distribution at the maximum temperature encountered in the system. Thanks to the RAINIER solver, studies of accurate radiative energy transfer in DNS or LES have become affordable recently [50, 51, 48]. In the present study, the local control of the Monte-Carlo convergence is set such that the results' standard deviation is either below 10% or, for points with small radiative contributions, below 3% of the maximum radiative power value. Additionally, fixing an upper threshold for the total number of rays per points allows not to spend computational efforts in irrelevant points such as those with negligible contribution to the radiative energy transfer. After carrying out several standalone radiation computations to determine this threshold, a maximum number of 4,000 rays per point was determined to allow matching of the convergence criteria for 99.9% of the points.

3.2.3 Wall heat transfer solver

Conjugate heat transfer is taken into account by solving the heat conduction within the solid parts of the combustion chamber. Only the four quartz windows that constitute the chamber walls are discretized. The temperature of the bottom wall that corresponds to the swirled injection exit plane is fixed in the reactive flow simulation from thermocouple measurements: the bottom plane temperature is taken as a linear profile, function of the radial distance from the chamber centerline, which varies from 450 K at the center to 550 K at the combustor corners. The physical properties of the quartz (type GE-124) are taken as $c_{p_s} = 954$ J/kg/K, $\rho_s = 2200$ kg/m^3 and $\lambda_s = 1.52$ W/m/K. The windows dimensions are: 250 mm (height) x 92 mm (width) x 12 mm (thickness).

As explained in section 2.2 about the accelerated coupling procedure, two heat transfer fields are considered: the first one from the unsteady heat equation, the second one from the steady heat equation. Both are actually solved by two instances of the YALES2 library and hence share the same data structure and discretization schemes as the flow solver: The unsteady heat transfer solver is then a finite volume solver using fourth-order schemes for space discretization and explicit time integration; Regarding the steady heat transfer solver, the linear system obtained by fourth-order spatial discretization of the steady heat equation is solved with the same parallel algorithm [30] as for the pressure Poisson equation.

Boundary conditions for quartz walls are provided on the internal side coupled with the reactive flow solver following the coupling procedure (see next section) and on the external side in contact with ambient air at the temperature $T_{ext} = 293$ K.

The contribution from the external free convection boundary layer being rather moderate, one must not forget the radiative flux on the external side. Given the hot wall temperature, the radiative heat flux cannot be linearized. The expression of the external wall heat flux ϕ_{bnd}^{ext} provides then a mixed boundary condition accounting for both free convection and radiative transfer,

$$\phi_{bnd}^{ext} = h_{ext}(T_{bnd} - T_{ext}) + \epsilon_{bnd}\sigma(T_{bnd}^4 - T_{ext}^4) \tag{10}$$

where natural convection is described by the heat transfer coefficient $h_{ext}(z)$, ϵ_{bnd} is the wall emissivity, and σ is the Stefan-Boltzmann constant. Quartz material is a semi-transparent medium that is transparent in the visible spectrum and becomes opaque in the infrared. Very detailed simulations should account for the corresponding spectral dependency of the quartz absorption coefficient. However, such data is not well known since the optical properties of quartz walls depends on the type of quartz, the manufacturing process and the temperature. For practical computations, a total hemispherical emissivity is usually considered instead. This is the approach chosen in the present study. A value of 0.75 is chosen for the wall emissivity that is relevant for a 2-cm-wide high-temperature window [15]. Given the laminar regime of the external free-convection boundary layer, $h_{ext}(z)$ is given by the Nusselt number expressed as $\mathrm{Nu}(z) = 0.39\,\mathrm{Ra}^{1/4}$ with the Rayleigh number Ra. Accounting for the 2-cm-wide plate below the quartz windows, an origin $z_0 = 2$ cm is introduced such that

$$h_{ext}(z) = \frac{\mathrm{Nu}(z - z_0)\lambda_{air}}{z - z_0}. \tag{11}$$

Air properties used to compute λ_{air} and the Rayleigh number are taken at a film temperature $T_m = 0.5(T_{ext} + T_{bnd})$. The sensitivity to the value of $h_{ext}(z)$ determined by Eq. 11 is studied in a simple manner by considering a 1D 12-mm-thick quartz layer with an imposed heat flux on the inner side ($\phi_0 = 3.5$ kW/m^2). The chosen value of ϕ_0 corresponds to the level of the wall conductive heat flux in the region investigated experimentally (see Fig. 13). The outer boundary condition used is the one prescribed by Eq. 11 for different values of the convective heat coefficient h_{ext}. As it can be seen in Fig. 7, modifying h_{ext} by 10% only causes a 1% variation in the inner wall temperature. Hence, the influence of the external convective heat coefficient on the wall temperature is small.

For the linear steady heat transfer solver, the resolution must be adapted to the non-linear boundary condition in Eq. 10. An outer iterative method (Fig. 8) with a fixed point algorithm is used on the external boundary temperature field. Within each outer iteration, the linear steady solver is applied to the linearized system where the radiative component is written as $T_{bnd}^4 \approx T_{bnd} \cdot (T_{bnd}^{est})^3$ to provide a new value for T_{bnd}. T_{bnd}^{est} is an estimation of the converged value of the external wall temperature which is updated after each iteration. This is repeated until the convergence is reached for the external boundary temperature field, which corresponds to the solution of the original non-linear heat transfer problem. Considering the solution converged when the variations between outer iterations are less than 5% yields an average number of five outer iterations in the studied case.

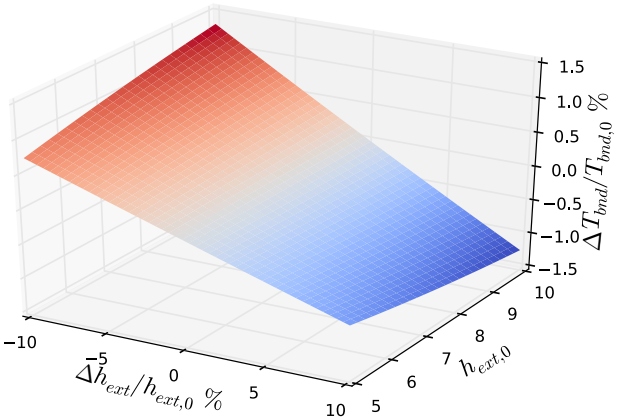

Fig. 7 Result of the 1D parametric study to quantify the sensitivity to the h_{ext} value: Surface plot of the resulting relative variation in the inner wall temperature T_{bnd} as a function to a reference value $h_{ext,0}$ and its relative variation.

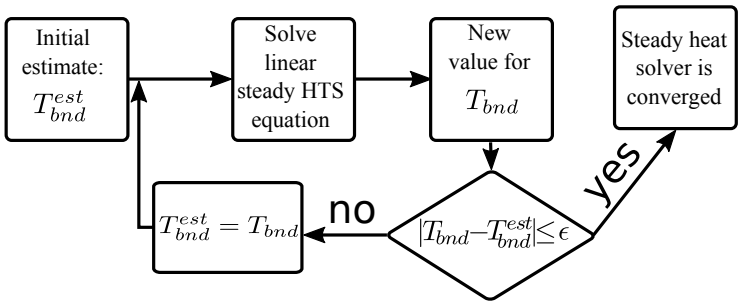

Fig. 8 Control loop for the fixed point algorithm used to solve the steady heat transfer equation when a radiative boundary condition is applied.

3.3 Coupling procedure

Multi-physics simulations are carried out by coupling the aforementioned solvers. All exchanged data between solvers are communicated with the coupling library OpenPALM [4] developed specifically for massively parallel coupled simulations.

The coupling between the reactive LES and wall heat transfer solvers, which enables simulations of conjugate heat transfer, is carried out with the accelerated HCND coupling method detailed in Sec. 2. The method computes accurately steady state fields without perturbing the unsteady contributions whose accuracy is controlled with a self-adaptive coupling period.

Accounting for radiative energy transfer introduces another coupling with the large-eddy simulation solver. The radiative energy transfer due to burnt gases and the combustor walls (internal side) is accounted for by coupling the Monte-Carlo solver to the reactive flow solver. The flow solver sends the gaseous mixture composition, the gaseous temperature field and the wall temperature field (obtained from

the heat transfer solver) to the radiative transfer solver. The Monte-Carlo solver then returns the volume radiative power which is used as a local source term in the gaseous enthalpy equation, and the wall radiative flux $\Phi_{rad,bnd}$ which is added to the heat flux $\Phi_{f,bnd}$ whose contributions are sent to the boundary temperature solver and the steady heat transfer solver. The communication scheme between solvers is presented in Fig. 9. To be affordable with the available computational

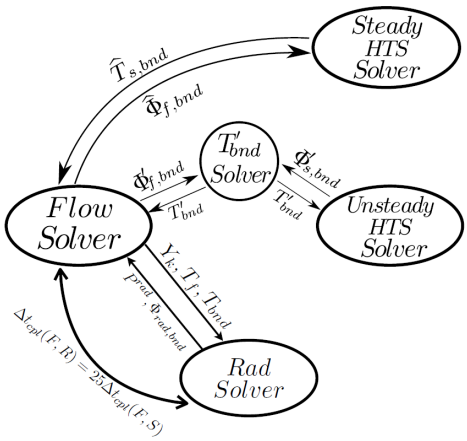

Fig. 9 Communication scheme of exchanged data for the coupling between the radiative transfer solver, the reactive flow solver and the wall heat transfer solvers

ressources, the radiative transfer equation is solved on a coarser mesh compared to the flow solver (see Tab. 2). The interpolation between meshes is handled by the OpenPalm coupling library. A dynamic coupling adaptation as not been derived yet for multi-physics simulations with radiation. The reactive flow and radiative transfer codes are then coupled with a fixed coupling time step, $\Delta t_{cpl}(F,R)$, related to the flow-wall coupling time $\Delta t_{cpl}(F,S)$ such that $\Delta t_{cpl}(F,R) = 25\Delta t_{cpl}(F,S)$. The period has been chosen to make affordable the coupled simulations with the considered coarser mesh.

4 Results for the studied confined premixed swirling flame and discussion

4.1 Presentation of CASE-FW and CASE-FWR

Results are presented for two coupled simulations: The first one considers coupled effects between the reactive flow and the walls heat transfer (denoted as CASE-FW), while the second additionally accounts for radiation (denoted as CASE-FWR). Let us outline once again that the numerical (discretization scheme and mesh) and modeling (subgrid and combustion model) setup of the LES solver is identical to the one in [33]. In this previous study, the measured wall temperature was prescribed in the simulation and the modeling setup was shown to retrieve

Table 2 Mesh size (in millions of cells) and number of cores used by each code for both the flow-wall coupled case and the flow-wall-radiation coupled case.

	CASE-FW		CASE-FWR	
	Mesh size	#CPUs	Mesh size	#CPUs
Reactive LES	49M	960	49M	256
Wall heat transfer	41M	95	41M	48
Radiation	-	-	8M	991

the impact of heat losses on the studied turbulent flame. The objective of the present study, highlighted in Sec. 1, is to estimate the wall heat losses without prior experimental knowledge, which translates into predicting accurately the wall temperature fields.

As shown later, the predicted wall temperature field is close to the experimental one, which was previously imposed in the stand-alone LES study in [33]. The predicted fields characterizing the reactive gaseous flow inside the chamber (flame shape, velocity profiles) are accordingly observed to be very similar between the present coupled results and the previous uncoupled ones. The velocity profiles are for example shown in Fig. 10. The agreement with experimental data is good. An asymmetry for both numerical profiles is noticed at the height of 25 mm which can be attributed either to experimental uncertainties or remaining modeling errors of the turbulent reactive flow. The overlapping of both numerical sets of velocity profiles indicates that, for the investigated configuration, it is adequate to impose the measured wall temperature in a stand-alone reactive LES to assess models that account for effects of heat losses on the flame. The next comparison with experimental measurements focuses on wall temperature which is essential to predict from coupled multiphysics simulations.

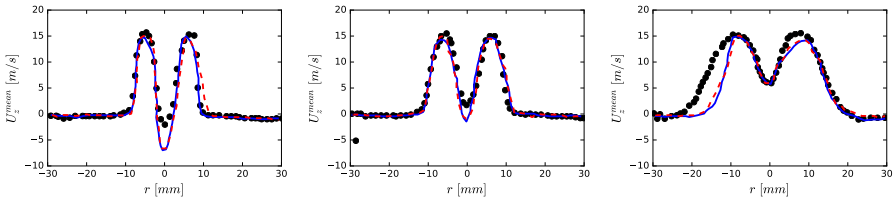

Fig. 10 Radial profiles of mean longitudinal velocity at different heights (left: 5 mm, middle: 10 mm, right: 25 mm) in the combustor. Symbols: Experimental data [33]. Solid blue line: Numerical results from [33] for the stand-alone LES with imposed wall temperature. Dashed red line: Numerical results of the coupled simulation CASE-FWR.

The different mesh size and number of cores for each solver in both simulations are given in Tab. 2. For both coupled cases, one core is used for the coupling code OpenPalm. The total number of cores is then 1,056 for CASE-FW and 1,296 for CASE-FWR. Accounting for the communications latency and exchanges, and for the interpolation of data between different meshes when accounting for radiation, CASE-FW is approximatively 15% more expensive computationally than the stand-alone uncoupled LES for the same computed physical time, while CASE-

FWR is 8.5 times more expensive than CASE-FW.
The simulation of CASE-FWR has been initiated with the final solution of CASE-FW. On the other hand, CASE-FW has been initiated from an instantaneous solution field from the statistically converged LES from Ref. [33]. In terms of characteristic time scale of the combustor $\tau = H/U = 18$ ms (where U is the bulk velocity in the injector), the sampling used for statistics computation is $10\,\tau$ in CASE-FW and $0.6\,\tau$ in CASE-FWR. The sampling procedure begins after 4 flow-through times τ for CASE-FW and 4.5 τ for CASE-FWR from their respective initial solutions. Because of the computational cost of CASE-FWR, its sampling duration is quite limited but it has been preferred to significantly decrease the time correlation between CASE-FW and CASE-FWR by simulating 4.5 τ of physical time before the sampling procedure. For CASE-FW, the total computational cost of the simulation is 350 thousand hours on a supercomputing cluster equipped with Intel E5-2690 processors, while for CASE-FWR the cost is of approximatively 1 million hours.

An example of the self-adaptive coupling time step computed in CASE-FW is presented in Fig. 11. The chosen error tolerance for the numerical integration is taken as $\eta = 5\%$. The obtained coupling time step has a mean value of approximatively 9 times the flow solver time step. This value is one order of magnitude below the stability limit of the coupling algorithm between the flow solver and the heat transfer solver. The advantage of the self-adaptive coupling time step enables not to *a priori* fix this parameter. A similar methodology for the coupling with thermal radiation remains to be developed.

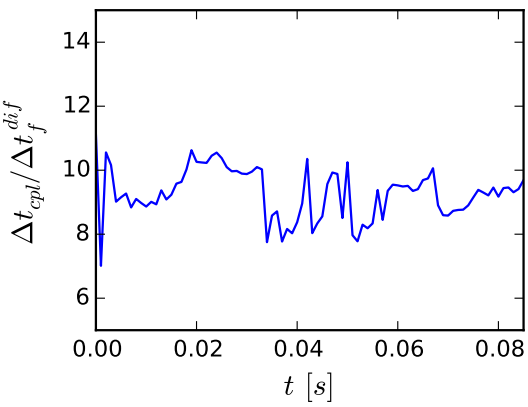

Fig. 11 Temporal evolution of the self-adaptive coupling time step scaled by the flow solver diffusive time step, for flow-wall coupling (CASE-FW), with time origin taken at the begining of the run. Error tolerance is set to $\eta = 5\%$ for the HCND control algorithm.

4.2 Wall temperature predictions

The computed reactive flow is shown in Fig. 12. It is similar for both studied cases. The mean velocity field shows that the swirled injected flow generates a central recirculation zone as well as external ones. The zone A is located at the bottom of the chamber while the second external recirculation zone (B) is much longer. The extent of recirculation B is roughly three fourth of the chamber height. A large volume of cooled burnt gases recirculates then towards the flame which is compact compared to the chamber's size. The progress variable reaction rate reveals that the dilution of the flame with such cold burnt gases damps the reaction zone in the swirled-flow outer shear layer. This effect can be accounted for thanks to the employed combustion model. Close to the combustor centerline, the burnt gases temperature is close to the adiabatic one just downstream the turbulent flame. Then, the hotter gases emit radiative energy (when radiation is considered) and mixes with the recirculating colder gases.

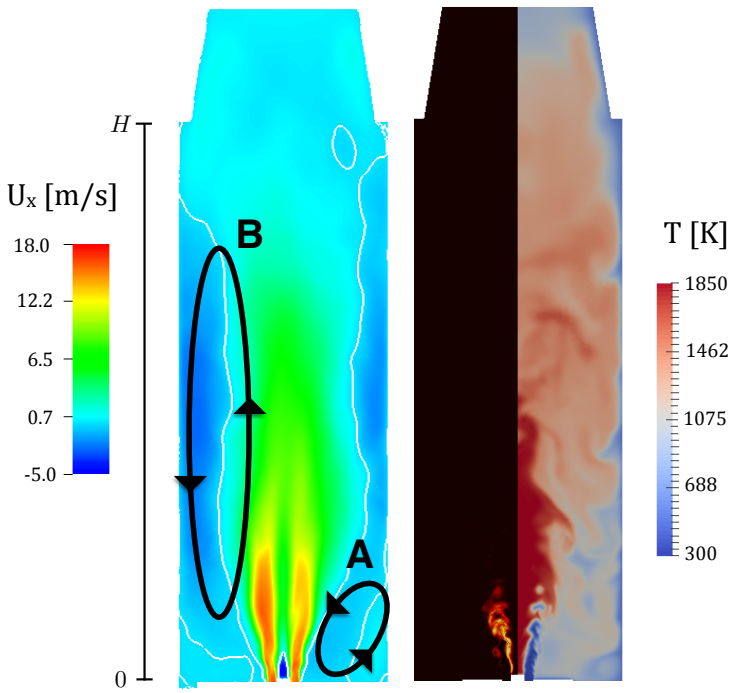

Fig. 12 Visualization of fields on the center plane for CASE-FWR. Left: Mean longitudinal velocity with the recirculation zones highlighted by the white iso-contour $U_x = 0$. Right: Instantaneous progress variable reaction rate (left half-domain, from zero in black and its maximum value in yellow) and temperature (right half-domain)

The large recirculating zone B prevents the direct contact of the hottest gases with the wall. The resulting wall temperature and conductive flux is shown in Fig. 13. The wall temperature and heat flux peak in the upper part of the recir-

culation B. Below, as the burnt gases get colder, the wall temperature decreases correspondingly. Finally, in the lowest zone, burnt gases are the coldest. This is accentuated by the slow recirculation zone A characterized by a large residence time and by the increased external heat transfer coefficient (Eq. 11) close to the chamber basis.

Laser Induced Phosphorescence (LIP) measurements of temperature (in the dotted white zone in Fig. 13) from [33] are compared to the computed fields in Fig. 14. Such LIP measurements are less invasive than arrays of thermocouples and are characterized by a 1% accuracy [3]. Without accounting for radiation, CASE-FW (middle figure) already provides a good agreement with the experimental values with a maximal local error of approximatively 10%. This level of agreement seems to indicate that the radiation is not strongly significant in this configuration of moderate size in atmospheric pressure conditions. A finer analysis in Sec. 4.3 will come to counter such a conclusion. The similar shape of iso-lines shows that the simulated reactive flow provided by the numerical and modeling approach described in Ref. [33] is well described with its characteristics: recirculation zones and swirling motion.

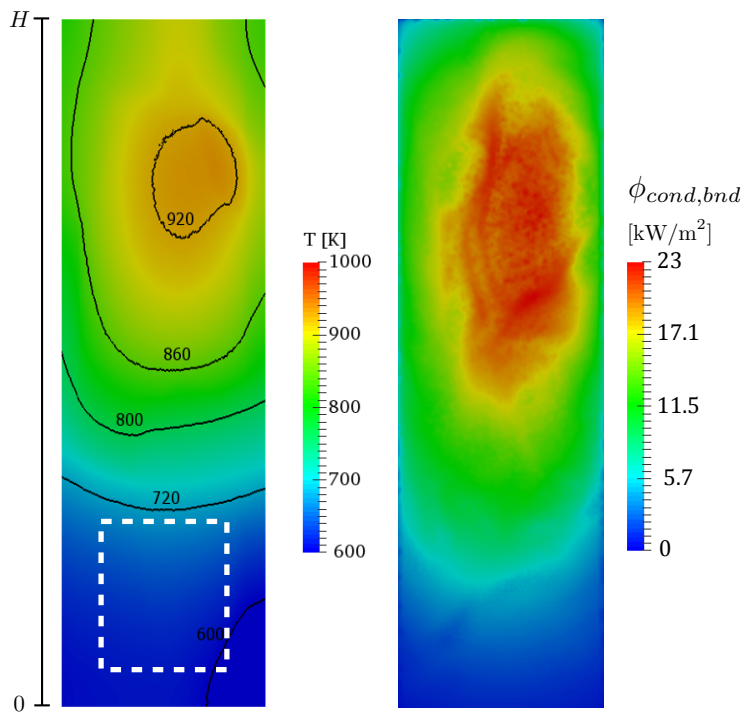

Fig. 13 Left: Quartz mean wall temperature predicted in CASE-FW. The dotted white rectangle represents the zone of LIP measurements. Right: Corresponding mean wall conductive flux

When radiation from burnt gases and quartz walls is taken into account, CASE-FWR (bottom of Fig. 14) shows numerical predictions which are noticeably improved with a maximal local error of about 3%. The previous underestimation of the wall temperature is then due to the neglected radiative effects. The observed level of agreement is truly impressive and has been achieved thanks to the derived high-fidelity multiphysics framework.

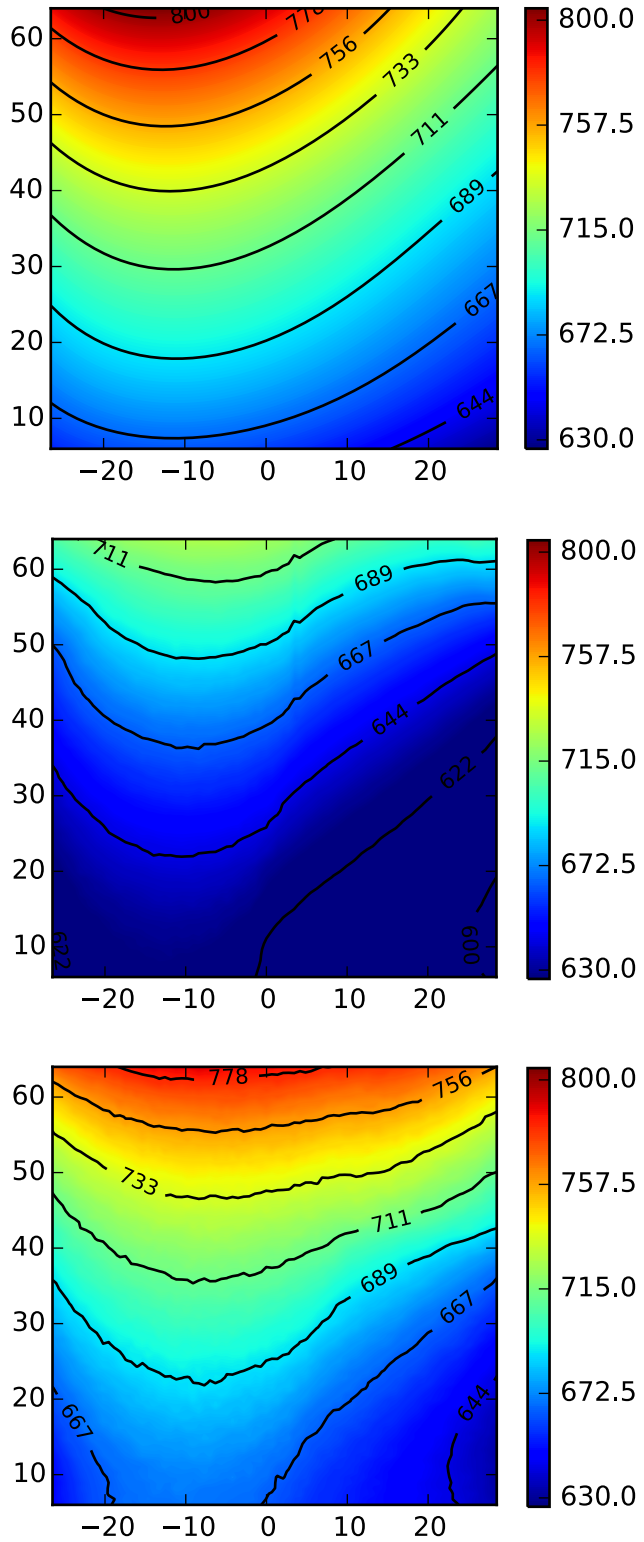

Fig. 14 Wall temperature (in Kelvin) over the measurements zone: $y \in [-24.5,\ 26.5]$, $z \in [6,\ 64]$, lengths in mm. Top: experimentally measured temperature values [33]. Middle: numerically computed wall temperature for CASE-FW. Bottom: numerically computed wall temperature for CASE-FWR.

4.3 Analysis of radiative effects

Snapshots of a temperature field and the corresponding radiative power are presented in Fig. 15. The local radiative power is written as: $P^{rad} = P_a^{rad} - P_e^{rad}$ where P_a^{rad} and P_e^{rad} are the absorbed and emitted radiative power, respectively. The middle subfigure only shows the emitted radiative power ($-P_e^{rad}$ is plotted) which is showed to be larger in magnitude than the actual one (bottom figure) accounting for both emission and absorption. This difference outlines that an optically thin assumption that would neglect absorption phenomena for all the spectrum wavelength is wrong in the present case and that the detailed radiative transfer equation must be solved.

The difference of mean gaseous temperature for cases CASE-FW and CASE-FWR is shown in the center plane in Fig. 16. The temperature maximum remains the same because the sudden temperature increase through the flame front is only marginally impacted by radiation. In the rest of the chamber, the radiative energy transfer homogenizes the temperature differences as also noticed in multi-physics simulations of a helicopter chamber [2]. Downstream the flame, hot burnt gases are seen to be colder when radiation is taken into account. This is outlined by the noticeable difference for the $T = 1400$ K iso-line. On the other hand, the cold burnt gases at the bottom of the chamber are hotter for CASE-FWR because of the radiation absorbed by the walls which yields a higher wall temperature (seen previously in Fig. 14). The $T = 1400$ K iso-line which is more irregular in CASE-FWR compared to CASE-FW outlines that CASE-FWR is not as well statistically converged as CASE-FW. This is also noticeable in the wall conductive flux shown in Fig. 17. Getting smoother converged fields would have required an additional 1 or 2 million cpu hours consumption which could not be afforded.

The resulting wall radiative and conductive flux for CASE-FWR are presented in Fig. 17. The wall radiative flux is seen to be of the same order of magnitude as the wall conductive flux, also seen in [2]. The ratio of wall-integrated (quartz walls only) conductive flux and total flux,

$$\frac{\int_w \phi_{cond,bnd} dS}{\int_w (\phi_{cond,bnd} dS + \int_w \phi_{rad,bnd}) dS}, \tag{12}$$

leads to a global value of 0.53. Estimating correctly the heat losses to the walls then requires to describe the radiative energy transfer. This conclusion seems contradictory to the relatively fair results obtained by CASE-FW to predict the wall temperature.

Let us explain this: Thermal radiation is an additional energy transfer mechanism that attenuate temperature differences between gas cells and also between the gas temperature and the wall temperature. Hence, when radiation is included, it is expected that the walls become hotter (see Fig. 14) while the burnt gases become cooler (see Fig. 16). After the thermal transient, the reduced temperature difference between the burnt gases and the walls induce a reduced wall conductive flux. Indeed, comparing the wall conductive flux for case FW (Fig. 13 right) and FWR (Fig. 17 bottom) shows that the wall flux is roughly halved when considering radiation. In case FWR, the reduced wall conductive flux is compensated by an additional contribution from the wall radiative flux. This feed-back loop of radiative transfer on the wall conductive flux explains why the total wall fluxes

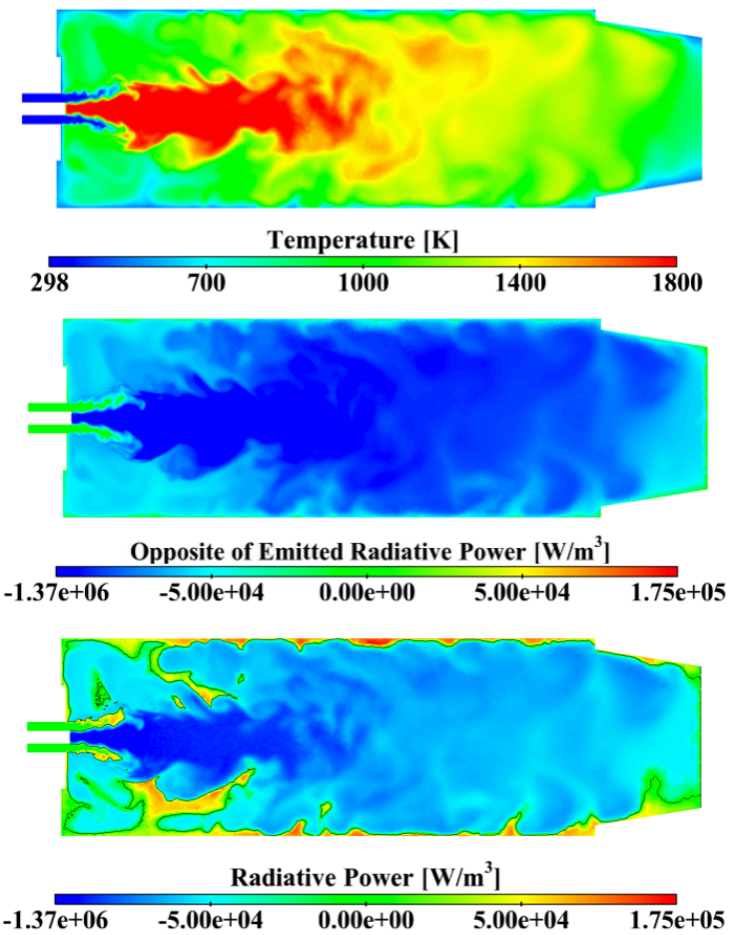

Fig. 15 Top: Instantaneous temperature field on the center plane. Middle: Radiative power $-P_e^{rad}$ (emission only). Bottom: Radiative power $P^{rad} = P_a^{rad} - P_e^{rad}$ with emission and absorption accounted for.

in the case FWR is not simply the conductive flux from the case FW with an additional contribution due to the radiation.

What remains surprising is the fact that the compensation from this feed-back loop lead roughly to the same wall temperature although the nature of the wall fluxes in the case FWR is so different. This is because, in the studied configuration, the CASE-FW conductive heat flux, which is overestimated compared to reality, surprisingly roughly accounts for the total wall heat flux (radiative and conductive) in case FWR.

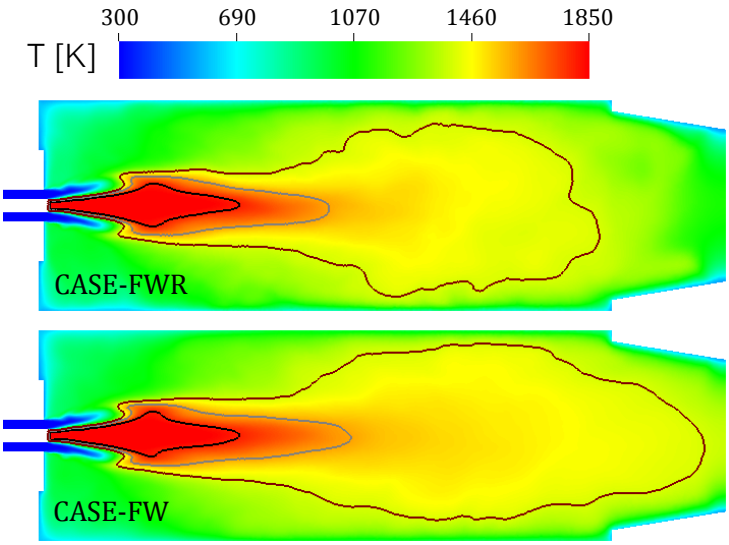

Fig. 16 Mean temperature on center plane for CASE-FWR (top) and CASE-FW (bottom). Iso-lines are given for T=1800 K (black solid line), T=1600 K (gray solid line) and T=1400 K (brown solid line).

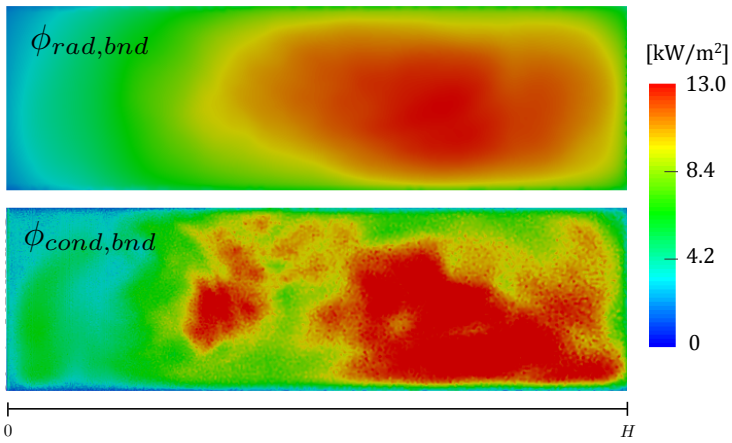

Fig. 17 Wall radiative (top) and conductive (bottom) heat flux for CASE-FWR.

This effect is clearly seen in the global energy budget of the combustor, expressed as a macroscopic balance of sensible enthalpy:

$$\underbrace{\int_{outlet} \rho u h_s dS}_{I} \underbrace{- \int_{inlet} \rho u h_s dS}_{II} + \underbrace{\int_{walls} \phi_{cond,bnd} dS}_{III} + \underbrace{\int_{walls} \phi_{rad,bnd} dS}_{IV} \underbrace{- \dot{\Omega}}_{V} = 0 \tag{13}$$

The different terms are the outlet convective flux (I), the value of inlet convective flux (II), the integrated wall conductive (III) and radiative (IV when considered) fluxes, and the opposite of the integrated heat release rate (V). Integrated wall fluxes account for the quartz windows and the bottom plane of the combustor whose temperature has been fixed. The budgets for cases FW and FWR are presented in Fig. 18. The comparison shows that the volume integrated heat release rate is effectively equal to 4 kW which is the burner theoretical power, showing that in both simulations the total amount of fuel is burnt. For CASE-FW around 35 % of the produced thermal energy is lost through wall heat flux by conduction only, while for CASE-FWR it is nearly 50 % for the sum of radiative and conductive contributions. For both cases, a substantial portion is then lost.

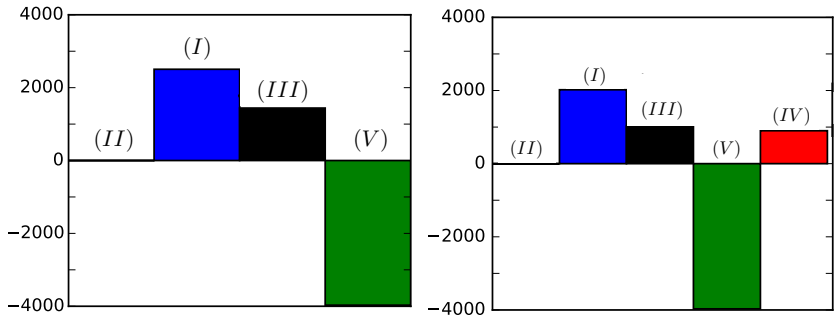

Fig. 18 Energy budget of the combustor for both CASE-FW (left) and CASE-FWR (right). Plotted variables are the inlet sensible enthalpy flow rate (II: gray), outlet sensible enthalpy flow rate (I: blue), conductive wall heat flux (III: black), volume-integrated heat release rate (V: green) and wall radiative flux (IV: red).

4.4 Wall fluctuations

The detailed unsteady multiphysics simulation enables to study the temporal variations in temperature and heat fluxes at the walls. The access to this unsteady thermal load on the combustor walls is necessary to later assess the thermal fatigue.

Figure 19 shows root-mean-square fields in the experimentally studied window for CASE-FW and CASE-FWR. In CASE-FW, the fluctuations in wall temperature and wall conductive flux present a similar pattern, highlighting the correlation between both quantities as also deduced from Eq. 6. The level of relative variation in the considered zone is approximatively 20% for the wall conductive flux and a little less than 1% for the wall temperature.

In CASE-FWR, the observed maximum value of wall temperature RMS is reduced but the field is more homogeneous, yielding a similar average level of relative variations ($\approx$ 1%). Similarly, with a roughly similar level of variations ($\approx$ 20%), the RMS in wall conductive flux is larger in CASE-FWR because of the increased steady wall conductive flux in the observed zone. Finally, the amplitude of variations in wall radiative flux is around 8%. Compared to CASE-FW, no

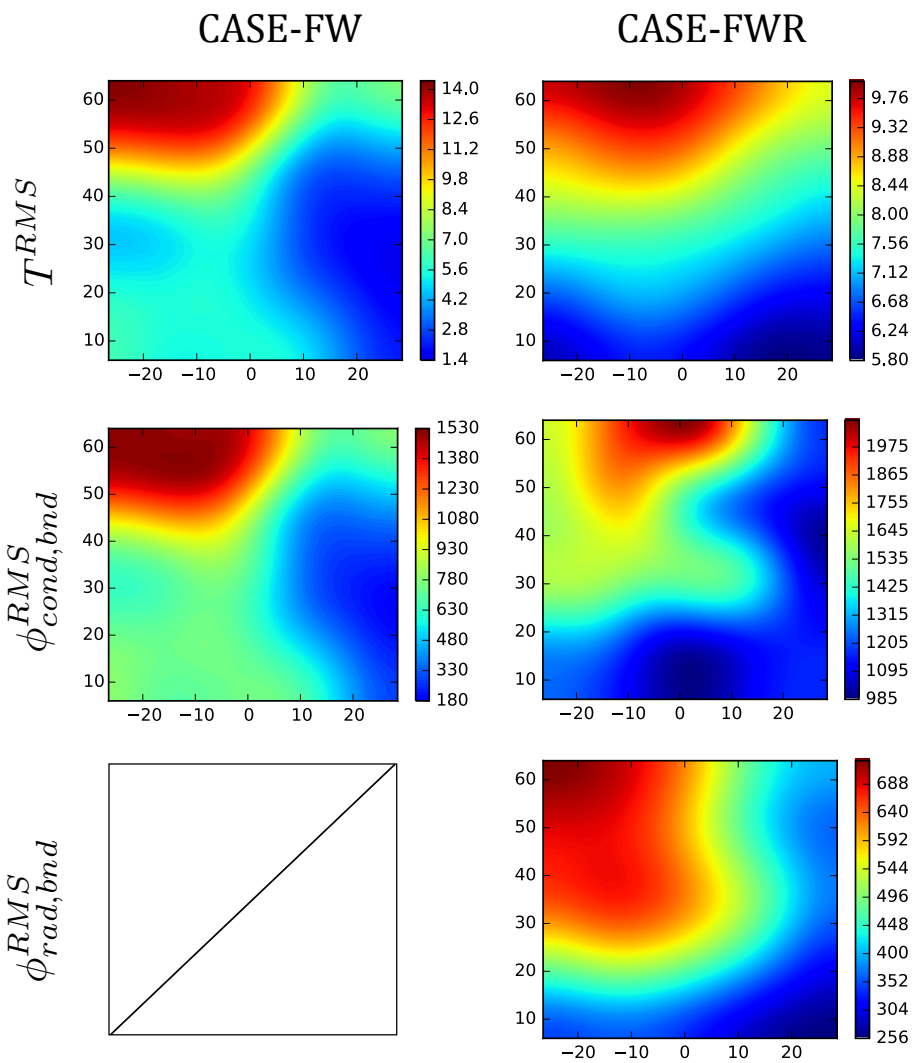

Fig. 19 RMS of wall temperature [K] (top), wall conductive heat flux [W/m^2] (middle) and wall radiative flux [W/m^2] (bottom) for cases CASE-FW (left column) and CASE-FWR (right column).

clear correlation appears between the RMS in wall temperature and either of the wall fluxes. Further analysis will deal with frequency-domain correlation studies to better understand the relationship between these quantities.

5 Conclusion

This study presents a state-of-the-art multiphysics simulation framework combining i) large-eddy simulation, ii) an efficient Monte-Carlo solver with detailed radiative properties and controlled accuracy, and iii) a self-adaptive coupling procedure for conjugate heat transfer to compute accurately steady and unsteady components of the solid domain temperature. The latter coupling approach derives from the Hybrid-Cell Neumann-Dirichlet method that allows an automatic determination of the coupling time step to adapt the temporal resolution to the studied configuration. The method has been first enhanced to determine permanent regime statistics with an acceleration method to artificially accelerate the transient slow heat conduction in the solid without impacting the studied fluctuations of wall temperature and heat flux. The resulting high-fidelity coupled simulation is applied to a confined premixed swirling flame under atmospheric pressure to predict the wall temperature measured experimentally by Laser Induced Phosphorescence. While always considering conjugate heat transfer, the coupled simulation is carried out with or without accounting for radiative energy transfer. Results yield a satisfactory agreement ($\approx 10\%$) without radiation which drops below 3% when detailed radiation is taken into account. Analysis of these results shows that radiation strongly modifies the balance of the macroscopic energy budget in the combustor. Hence, concluding from the case without radiation that the wall conductive heat flux is dominant over the radiative one is solid wrong. The unsteadiness of wall temperature and heat fluxes is finally compared between both simulations, showing similarities and differences which shall need further analysis for a better understanding.

The combined experimental and numerical characterization of combustion and heat transfer as carried out by [18, 17] in a confined turbulent flame is recent and similar future studies are necessary to further assess the accuracy of multi-physics simulations. A more complete validation will benefit for example from the measure of wall temperature on both sides along with the exhaust gases temperature. This would provide additional data in terms of wall total heat fluxes and the global amount of heat losses. Similarly, additional experimental data on unsteadiness at combustors' walls are necessary to validate the estimated RMS fields.

Besides achieving accurate predictions, one of the objective of such high-fidelity simulations is their comparison with simpler approaches and low-order models. Because of their large computational cost, they are not affordable in a design optimization loop for example. The obtained reference results on a couple of operating conditions and/or different geometries can be used to either calibrate other models or identify the origin of their lack of accuracy and possibly remedy it. Nonetheless, the proposed kind of computationally intensive coupled simulations still relies on models and methods that introduce some errors and uncertainties in the results. It is therefore still necessary to assess and improve these models and methods. For example, the implications of the coupling period and of the use of a coarser mesh for the radiative transfer solver must be characterized in future studies. Another aspect moderating the accuracy of the presented approach is the neglect of the effects of subgrid fluctuations in the resolved radiative transfer equation. Such effects combined with the lower spatial and temporal resolution will have to be quantified. Laboratory experimental setups being equipped with windows for

optical access, the impact of the semitransparent property of such boundaries on the global heat transfer balance will have to be accounted for as well.

Acknowledgements We acknowledge the ASME for granting the permission to include the original material from Refs. [25,26] to assemble the present article. This work was supported by the Air Liquide, CentraleSupélec and CNRS Chair on oxycombustion and heat transfer for energy and environment and by the OXYTEC project, grant ANR-12-CHIN-0001 of the French Agence Nationale de la Recherche. This work was granted access to the HPC resources of CINES under the allocation 2015-x20142b0164 made by GENCI. Vincent Moureau and Ghislain Lartigue from CORIA, and the SUCCESS scientific group are acknowledged for providing the YALES2 code. Thibault Guiberti and Adrien Chatelier are also acknowledged for discussions concerning the experimental setup and measurements.

Compliance with Ethical Standards

Conflict of interests The authors declare that they have no conflict of interest.

References

1. Auzillon, P., Gicquel, O., Darabiha, N., Veynante, D., Fiorina, B.: A filtered tabulated chemistry model for les of stratified flames. Combustion and Flame **159**(8), 2704–2717 (2012)
2. Berger, S., Richard, S., Duchaine, F., Staffelbach, G., Gicquel, L.Y.M.: On the sensitivity of a helicopter combustor wall temperature to convective and radiative thermal loads. Applied Thermal Engineering **103**, 1450–1459 (2016)
3. Brübach, J., Pflitsch, C., Dreizler, A., Atakan, B.: On surface temperature measurements with thermographic phosphors: A review. Progress in Energy and Combustion Science **39**(1), 37–60 (2013)
4. Buis, S., Piacentini, A., Déclat, D.: Palm: a computational framework for assembling high-performance computing applications. Concurrency and Computation: Practice and Experience **18**(2), 231–245 (2006)
5. Charlette, F., Meneveau, C., Veynante, D.: A power-law flame wrinkling model for les of premixed turbulent combustion, part i: non-dynamic formulation. Combustion and Flame **131**(1/2), 159–180 (2002)
6. Coelho, P.J.: Numerical simulation of the interaction between turbulence and radiation in reactive flows. Progress in Energy and Combustion Science **33**, 311–383 (2007)
7. Coelho, P.J.: Turbulence-Radiation Interaction: From Theory to Application in Numerical Simulations. Journal of Heat Transfer-Transactions of the ASME **134**(3) (2012)
8. Donini, A., Martin, S., Bastiaans, R., van Oijen, J., de Goey, L.: Numerical simulations of a premixed turbulent confined jet flame using the flamelet generated manifold approach with heat loss inclusion. In: ASME Turbo Expo 2013: Turbine Technical Conference and Exposition, V01AT04A024. American Society of Mechanical Engineers (2013)
9. Duchaine, F., Corpron, A., Pons, L., Moureau, V., Nicoud, F., Poinsot, T.: Development and assessment of a coupled strategy for conjugate heat transfer with large eddy simulation: Application to a cooled turbine blade. International Journal of Heat and Fluid Flow **30**(6), 1129 – 1141 (2009)
10. Duchaine, F., Maheu, N., Moureau, V., Balarac, G., Moreau, S.: Large-eddy simulation and conjugate heat transfer around a low-mach turbine blade. Journal of Turbomachinery **136**(5), 051,015–051,015 (2013)
11. Errera, M.P., Chemin, S.: Optimal solutions of numerical interface conditions in fluid–structure thermal analysis. Journal of Computational Physics **245**, 431 – 455 (2013)
12. Fiorina, B., Mercier, R., Kuenne, G., Ketelheun, A., Avdić, A., Janicka, J., Geyer, D., Dreizler, A., Alenius, E., Duwig, C., et al.: Challenging modeling strategies for les of non-adiabatic turbulent stratified combustion. Combustion and Flame **162**(11), 4264–4282 (2015)

13. Fiorina, B., Vicquelin, R., Auzillon, P., Darabiha, N., Gicquel, O., Veynante, D.: A filtered tabulated chemistry model for les of premixed combustion. Combustion and Flame **157**(3), 465–475 (2010)
14. Galpin, J., Simoneau, J.: Large eddy simulation of a thermal mixing tee in order to assess the thermal fatigue. International Journal of Heat and Fluid Flow **32**(3), 539–545 (2011)
15. Gardon, R.: The emissivity of transparent materials. Journal of the American Ceramic Society **39**(8), 278–287 (1956)
16. Gicquel, L.Y.M., Staffelbach, G., Poinsot, T.: Large Eddy Simulations of gaseous flames in gas turbine combustion chambers. Progress in Energy and Combustion Science **38**(6), 782–817 (2012)
17. Guiberti, T., Durox, D., Scouflaire, P., Schuller, T.: Impact of heat loss and hydrogen enrichment on the shape of confined swirling flames. Proceedings of the Combustion Institute **35**(2), 1385–1392 (2015)
18. Guiberti, T.F., Durox, D., Zimmer, L., Schuller, T.: Analysis of topology transitions of swirl flames interacting with the combustor side wall. Combustion and Flame **162**(11), 4342–4357 (2015)
19. Gupta, A., Haworth, D., Modest, M.: Turbulence-radiation interactions in large-eddy simulations of luminous and nonluminous nonpremixed flames. Proceedings of the Combustion Institute **34**(1), 1281 – 1288 (2013)
20. He, L.: Fourier spectral modelling for multi-scale aero-thermal analysis. International Journal of Computational Fluid Dynamics **27**(2), 118–129 (2013)
21. He, L., Oldfield, M.: Unsteady conjugate heat transfer modelling. ASME Journal of Turbomachinery **133**(3), 031,022 (2011)
22. Jaure, S., Duchaine, F., Staffelbach, G., Gicquel, L.: Massively parallel conjugate heat transfer methods relying on large eddy simulation applied to an aeronautical combustor. Computational Science & Discovery **6**(1), 015,008 (2013)
23. Jones, W.P., Paul, M.C.: Combination of dom with les in a gas turbine combustor. International Journal of Engineering Science **43**(5–6), 379–397 (2005)
24. Ketelheun, A., Kuenne, G., Janicka, J.: Heat transfer modeling in the context of large eddy simulation of premixed combustion with tabulated chemistry. Flow, Turbulence and Combustion **91**(4), 867–893 (2013)
25. Koren, C., Vicquelin, R., Gicquel, O.: An acceleration method for numerical studies of conjugate heat transfer with a self-adaptive coupling time step method: Application to a wall-impinging flame (50893), V05CT17A006– (2017). URL http://dx.doi.org/10.1115/GT2017-64224
26. Koren, C., Vicquelin, R., Gicquel, O.: High-fidelity multiphysics simulation of a confined premixed swirling flame combining large-eddy simulation, wall heat conduction and radiative energy transfer (50893), V05CT17A010– (2017). URL http://dx.doi.org/10.1115/GT2017-64844
27. Koren, C., Vicquelin, R., Gicquel, O.: Self-adaptive coupling frequency for unsteady coupled conjugate heat transfer simulations. International Journal of Thermal Sciences **118**, 340–354 (2017)
28. Kuhn, S., Braillard, O., Ničeno, B., Prasser, H.M.: Computational study of conjugate heat transfer in t-junctions. Nuclear Engineering and Design **240**(6), 1548–1557 (2010)
29. Lee, J.I., Hu, L.w., Saha, P., Kazimi, M.S.: Numerical analysis of thermal striping induced high cycle thermal fatigue in a mixing tee. Nuclear Engineering and Design **239**(5), 833–839 (2009)
30. Malandain, M., Maheu, N., Moureau, V.: Optimization of the deflated conjugate gradient algorithm for the solving of elliptic equations on massively parallel machines. Journal of Computational Physics **238**, 32–47 (2013)
31. Mari, R., Cuenot, B., Rocchi, J.P., Selle, L., Duchaine, F.: Effect of pressure on hydrogen/oxygen coupled flame–wall interaction. Combustion and Flame **168**, 409–419 (2016)
32. Mercier, R., Auzillon, P., Moureau, V., Darabiha, N., Gicquel, O., Veynante, D., Fiorina, B.: Les modeling of the impact of heat losses and differential diffusion on turbulent stratified flame propagation: Application to the tu darmstadt stratified flame. Flow, turbulence and combustion **93**(2), 349–381 (2014)
33. Mercier, R., Guiberti, T., Chatelier, A., Durox, D., Gicquel, O., Darabiha, N., Schuller, T., Fiorina, B.: Experimental and numerical investigation of the influence of thermal boundary conditions on premixed swirling flame stabilization. Combustion and Flame **171**, 42–58 (2016)

34. Moin, P., Apte, S.V.: Large-eddy simulation of realistic gas turbine combustors. AIAA Journal **44**(4), 698–708 (2006)
35. Moureau, V., Domingo, P., Vervisch, L.: Design of a massively parallel cfd code for complex geometries. Comptes Rendus Mecanique **339**(2-3), 141–148 (2011)
36. Nicoud, F., Ducros, F.: Subgrid-scale stress modelling based on the square of the velocity gradient tensor. Flow, Turbulence and Combustion **62**(3), 183–200 (1999)
37. Nicoud, F., Toda, H.B., Cabrit, O., Bose, S., Lee, J.: Using singular values to build a subgrid-scale model for large eddy simulations. PHYSICS OF FLUIDS **23**(8) (2011). DOI 10.1063/1.3623274
38. Nogenmyr, K.J., Cao, H.J., Chan, C.K., Cheng, R.K.: Effects of confinement on premixed turbulent swirling flame using large eddy simulation. Combustion Theory and Modelling **17**(6), 1003–1019 (2013)
39. Poitou, D., Amaya, J., El Hafi, M., Cuénot, B.: Analysis of the interaction between turbulent combustion and thermal radiation using unsteady coupled les/dom simulations. Combustion and Flame **159**(4), 1605–1618 (2012)
40. Proch, F., Kempf, A.M.: Modeling heat loss effects in the large eddy simulation of a model gas turbine combustor with premixed flamelet generated manifolds. Proceedings of the Combustion Institute **35**(3), 3337–3345 (2015)
41. dos Santos, R.G., Lecanu, M., Ducruix, S., Gicquel, O., Iacona, E., Veynante, D.: Coupled large eddy simulations of turbulent combustion and radiative heat transfer. Combustion and Flame **152**(3), 387–400 (2008)
42. Söderlind, G.: Digital filters in adaptive time-stepping. ACM Transactions on Mathematical Software (TOMS) **29**(1), 1–26 (2003)
43. Soucasse, L., Riviere, P., Soufiani, A.: Subgrid-scale model for radiative transfer in turbulent participating media. Journal of Computational Physics **257**(A), 442–459 (2014)
44. Taine, J., Soufiani, A.: Gas ir radiative properties: From spectroscopic data to approximate models. pp. 295 – 414. Elsevier (1999)
45. Tay-Wo-Chong, L., Zellhuber, M., Komarek, T., Im, H.G., Polifke, W.: Combined influence of strain and heat loss on turbulent premixed flame stabilization. Flow, Turbulence and Combustion **97**(1), 263–294 (2016)
46. Tesse, L., Dupoirieux, F., Zamuner, B., Taine, J.: Radiative transfer in real gases using reciprocal and forward Monte Carlo methods and a correlated-k approach. International Journal of Heat and Mass Transfer **45**(13), 2797–2814 (2002)
47. Trisjono, P., Kleinheinz, K., Pitsch, H., Kang, S.: Large eddy simulation of stratified and sheared flames of a premixed turbulent stratified flame burner using a flamelet model with heat loss. Flow, Turbulence and Combustion **92**(1), 201–235 (2014)
48. Vicquelin, R., Zhang, Y.F., Gicquel, O., Taine, J.: Effects of radiation in turbulent channel flow: analysis of coupled direct numerical simulations. Journal of Fluid Mechanics **753**, 360–401 (2014)
49. Zhang, Y., Gicquel, O., Taine, J.: Optimized emission-based reciprocity monte carlo method to speed up computation in complex systems. International Journal of Heat and Mass Transfer **55**(25), 8172–8177 (2012)
50. Zhang, Y., Vicquelin, R., Gicquel, O., Taine, J.: Physical study of radiation effects on the boundary layer structure in a turbulent channel flow. International Journal of Heat and Mass Transfer **61**, 654–666 (2013)
51. Zhang, Y.F., Vicquelin, R., Gicquel, O., Taine, J.: A wall model for les accounting for radiation effects. International Journal of Heat and Mass Transfer **67**(0), 712–723 (2013)